ACS APPLIED MATERIALS & INTERFACES

Research Article

www.acsami.org

Order Induced Charge Carrier Mobility Enhancement in Columnar Liquid Crystal Diodes

Juliana Eccher,[†,‡] Gregório C. Faria,[§] Harald Bock,[⊥] Heinz von Seggern,[‡] and Ivan H. Bechtold*[,†]

[†]Departamento de Física, Universidade Federal de Santa Catarina−UFSC, 88040-900 Florianópolis, SC, Brazil

[‡]Department of Electronic Materials, Institute of Materials Science, Technical University of Darmstadt, Petersenstrasse 23, D-64287, Darmstadt, Germany

[§]Instituto de Física de São Carlos, Universidade de São Paulo, 13560-970 São Carlos, SP, Brazil

[⊥]Centre de Recherche Paul Pascal, Université de Bordeaux & CNRS, 115 Avenue Schweitzer, 33600 Pessac, France

Supporting Information

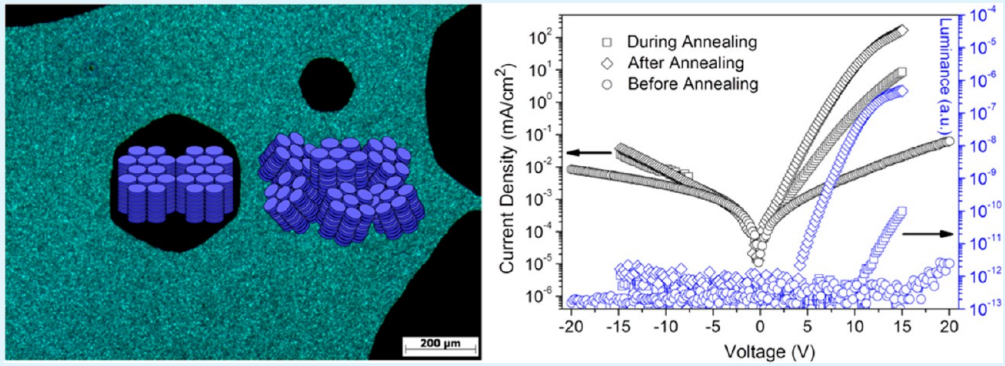

ABSTRACT: Discotic molecules comprising a rigid aromatic core and flexible side chains have been promisingly applied in OLEDs as self-organizing organic semiconductors. Due to their potentially high charge carrier mobility along the columns, device performance can be readily improved by proper alignment of columns throughout the bulk. In the present work, the charge mobility was increased by 5 orders of magnitude due to homeotropic columnar ordering induced by the boundary interfaces during thermal annealing in the mesophase. State-of-the-art diodes were fabricated using spin-coated films whose homeotropic alignment with formation of hexagonal germs was observed by polarizing optical microscopy. The photophysical properties showed drastic changes at the mesophase-isotropic transition, which is supported by the gain of order observed by X-ray diffraction. The electrical properties were investigated by modeling the current−voltage characteristics by a space-charge-limited current transport with a field dependent mobility.

KEYWORDS: *organic electronics, charge carrier mobility, columnar liquid crystals, perylenediimide, homeotropic alignment, interface effect*

1. INTRODUCTION

Organic charge-transporting materials have been intensively studied because of their potential application in electronic and optoelectronic devices such as organic field effect transistors (OFETs), organic light emitting diodes (OLEDs), and organic photovoltaic cells (OPVs).[1] In this respect liquid crystals (LCs) are currently being recognized as a new class of self-organizing organic semiconductors, which are characterized by high charge carrier mobility.[2] Whereas rod-like molecules give rise to smectic phases, in which the molecules are arranged in layers acting as 2D conductors, disc-like molecules may give rise to columnar phases, in which the molecules are stacked on top of one another resulting in columnar organization. Charge transport in these systems is "quasi one-dimensional" and occurs along these columns.[3] In the most common hexagonal columnar phase the columns are arranged on a regular two-dimensional hexagonal lattice.

Recently, columnar liquid crystals (ColLCs) have found increasing interest as a promising class of liquid crystal materials for electronic applications including OFETs, OLEDs, and OPVs.[4−6] The disk-like molecules form stable columns due to overlap of the π-orbitals of their aromatic core and side chain (tail) interactions, while thermal fluctuations of these tails give rise to the liquid-like dynamic disorder.[7] ColLCs form efficient $\pi-\pi$ columnar stacks that induce a high charge carrier mobility, which strongly depends on the degree of order and $\pi-\pi$ molecular orbital overlap within the columnar stacks. The

Received: August 29, 2013
Accepted: October 18, 2013
Published: November 5, 2013

organization of those columns increases the local order without creating many grain boundaries on the macroscopic level as in the case of crystalline materials. The reason for this can be found in the material's ability to self-heal structural defects due to their partially liquid-like character. Consequently, under simple thermal annealing, they usually can spontaneously form large single domains.[1,3,8,9] ColLC materials therefore combine several advantageous properties: long-range self-assembly, self-healing, visible light absorption, easy processing, high charge-carrier mobility, and tunable surface alignment of the column axes.[3,7]

The ability to control the macroscopic orientations of columnar superstructures on surfaces is critical to attain high charge-carrier mobility. There are two distinct uniform alignments of ColLCs: the planar uniaxial alignment with edge-on orientation of the molecules (column axes parallel to the substrate) and the homeotropic alignment with a face-on orientation of the discs (column axes perpendicular to the substrate). Unidirectional planar alignment is a priori ideal for OFETs, while the homeotropic alignment is ideal for OLED and OPV applications. The face-on orientation can occur during mesophase formation by slow cooling of the material from the isotropic phase.[3,5,10]

With respect to order, LCs have advantages over amorphous materials, and moreover, they allow tuning the degree of order in the bulk and at the interfaces when compared with crystalline materials. It has already been revealed that some discotic and smectic liquid crystals exhibit high mobilities ranging from 10^{-4} cm^2 V^{-1} s^{-1} up to 1 cm^2 V^{-1} s^{-1}.[2,8] For practical device applications a liquid-crystalline material must, besides featuring a high charge mobility, also exhibit a wide mesophase temperature range, including ambient temperatures.[11] On top of that, LC molecules can be designed to be soluble in common organic solvents, being easily processable from solution. Several recent review articles[2−5,9,10,12] have discussed the specific aspects and the advantages of LCs for potential use in OFETs, OLEDs, and OPVs, where in some cases special attention has been devoted to the alignment techniques that improve the performance of such devices.

Substituted phthalocyanines are a class of columnar mesogenic materials widely investigated as donor materials.[6,13] As acceptor materials, perylenediimides[8,14−17] and related molecules have been extensively studied due to their high electron affinity, making them highly attractive as n-type semiconductors with favorable absorption properties in the visible range. These perylene dye materials have also attracted much attention due to their high thermal and chemical stabilities.[18] Columnar perylene derivatives have been applied in OLEDs,[19,20]OFET,s[21−23] and OPVs.[24−26] They even have been utilized as electron transporting material in OLEDs based on two complementary ColLCs, a columnar donor and a columnar acceptor.[19,20] Compounds based on perylenediimide are among the best and most used n-type semiconductors.[27]

In this work, we show that the electrical properties of a perylenediimide derivative are dramatically improved by thermal annealing of a diode-like structure leading to homeotropic alignment. The current versus voltage (J/V) characteristics were analyzed in terms of an Ohmic behavior for low voltages and modeled for higher voltages by a space-charge-limited current transport with a field dependent mobility. In order to characterize the structural order as well as the morphology a multitechnique approach was used.

2. EXPERIMENTAL SECTION

The synthesis of the ColLC used here, benzo[*ghi*]perylene-1,2,4,5,10,11-hexacarboxylic 1,2-bis(2-ethylhexyl)ester 4,5:10,11-bis-(undec-4-yl)imide, has been published elsewhere.[28] The transition temperatures and associated enthalpies were determined by differential scanning calorimetry (DSC) using a TA equipment Q2000 module. The thermal gravimetric analysis (TGA) was made with a Shimadzu thermogravimetric analyzer TGA-50. A heating and cooling rate of 10 °C min^{-1} with a nitrogen flow of 50 mLmin^{-1} was used. The textures of the substance in its mesophase sandwiched between two glass slides were obtained from an Olympus BX50 polarizing optical microscope (POM) in transmission mode, equipped with a Mettler Toledo FP-82 hot stage to control the temperature. The images were recorded with a CCD camera coupled to the optical microscope.

The X-ray diffraction (XRD) experiments were performed using a X'PERT-PRO (PANalytical) diffractometer with CuKα radiation (λ = 1.5418 Å) performed in continuous scanning mode from 2° to 30° (2θ angle). The diffracted radiation was collected with an X'Celerator detector. The samples were prepared by heating the powder material on a glass plate to complete melting bringing them into the isotropic phase, followed by cooling to room temperature. As a result, a film of a thickness of approximately 1 mm was obtained. The film was then placed into a diffractometer on a TCU2000-Temperature Control Unit (Anton Paar). During measurement the film was heated up to the isotropic phase, and the diffraction patterns were collected during cooling back through the mesophase down to room temperature.

The absorption and fluorescence spectra were collected in the solid state with an OceanOptics USB4000 spectrophotometer. Measurements were performed on spin-coated films (at 2000 rpm for 30 s) using a 50 mg/mL n-heptane solution on glass substrates. To determine the absorption and the fluorescence as a function of the temperature, films were placed on a hot stage (Mettler Toledo FP-82) and illuminated with a UV lamp. The absorbance and emission spectra were captured using an optical fiber placed close to the film.

Atomic Force Microscopy (AFM) was performed on spin-coated films to determine their morphological properties, using a Nanosurf EasyScan2 apparatus in tapping mode with a scanning rate of 1.0 Hz covering 512 × 512 lines.

The energy level of the LUMO (lowest unoccupied molecular orbital) was obtained by cyclic voltammetry (CV) on a thin film. The voltammogram was recorded at a scan rate of 100 mV s^{-1} from a solution in acetonitrile containing 0.1 M tetrabutylammoniumhexafluorophosphate ($TBAPF_6$) as electrolyte. A three-electrode cell was used, with the ColLC coated on a platinum (Pt) electrode as the working electrode, a Pt wire as the counter electrode, and an Ag^+/AgCl electrode as reference. The potentials were corrected in relation to the ferrocene/ferrocenium (Fc/Fc^+) redox couple, used as internal standard. Before starting the measurements the cell was deoxygenated by purging with nitrogen gas. The optical band gap was determined from the absorption spectrum of a thin film. The HOMO (highest occupied molecular orbital) energy level was then estimated from the optical band gap and above determined LUMO level.

For the electrical characterization, diodes were fabricated by solution processing of the mesogenic material in n-heptane at a concentration of 50 mg/mL. ITO (indium tin-oxide) coated glass plates with sheet resistances of about 15 Ω/□ were used as conductive substrates. After proper substrate cleaning, a thin layer of PEDOT:PSS [poly(3,4-ethylenedioxythiophene) poly(styrenesulfonate)] was deposited by spin coating at 3000 rpm during 30 s, followed by annealing at 110 °C for 5 min. Then the mesogen-containing solution was spin-coated at 2000 rpm for 30 s. The thickness of the coated films was probed with a Dektak 8000 profilometer. Top electrodes were obtained by a sequential vacuum deposition (10^{-7} mbar) of Ca (50 nm) and Al (100 nm) at a deposition rate of 2 Å/s. The active area of the diode was 10 mm^2. Devices were annealed on a hot plate at 120 °C for three hours in order to achieve homeotropic alignment, followed by cooling to room temperature. The J/V curves were measured at room temperature (25 °C) using a HP Semiconductor Parameter Analyzer (Model 4145A). AC impedance measurements were

performed to determine the dielectric constant of the mesogenic material, using an Impedance/Gain-Phase Analyzer (SI 1260) in the frequency range of 0.1−10^6 Hz.

3. RESULTS AND DISCUSSION

Thermal Stability and Liquid Crystalline Properties. The thermal stability of the mesogenic material was evaluated by TGA measured under a nitrogen atmosphere, showing high stability with decomposition temperatures above 350 °C (see the Supporting Information). The material presented a hexagonal columnar liquid-crystalline mesophase (Col_h), characterized by POM and XRD.

Figure 1 shows the DSC measurement for a heating and cooling cycle. During heating, only one endothermic peak was observed with an onset at 151.2 °C, which is related to the transition from the liquid crystalline mesophase to the isotropic liquid state. During the cooling-down stage, the same peak was observed with onset at 150.1 °C, indicating the transition from the isotropic liquid state to the Col_h mesophase. The values for the transition enthalpies were around 8.8 kJ/mol (91.2 meV). No further phase transition was detected down to −50 °C, indicating that the mesophase is stable in a wide temperature range including room temperature, which is favorable for practical applications.

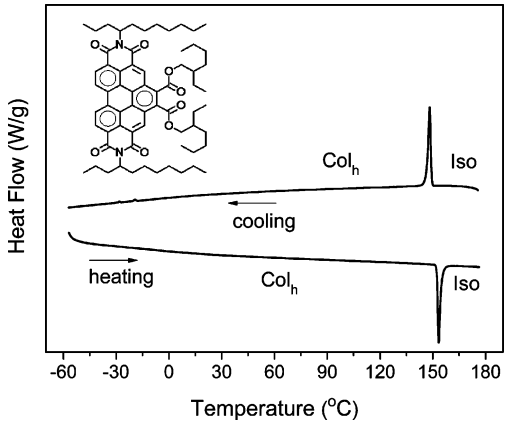

Figure 1. DSC heating and cooling cycles, using a rate of 10 °C min^{-1} with a nitrogen flow of 50 mL min^{-1}. Inset: scheme of the molecular structure of the mesogenic compound.

Textures typical for a Col_h mesophase were observed by POM as a function of temperature. They are very similar to those described elsewhere for materials based on the perylene core.[8] The textures were obtained by cooling down at a rate of 10 °C min^{-1} from the isotropic liquid state. Figure 2a shows the focal conic texture at 120 °C, which was similar to the one observed at room temperature, see Figure 2b, which confirms that the hexagonal columnar structure is maintained at room temperature.

To confirm the hexagonal columnar structure of the mesophase, XRD measurements as a function of temperature were performed. Figure 3 shows the temperature dependence of the first and second order X-ray diffraction peaks of the columnar lattice in the temperature range of the mesophase and, as inset, the overall X-ray diffraction patterns in the isotropic liquid phase and the mesophase. The presence of two well-defined nonsplit peaks in the low angle region at 2θ = 4.5° (100) and 2θ = 9.1° (200) leads, together with the optical texture, to the assignment of a hexagonal columnar mesophase with reciprocal spacing ratio of 1:2.[29,30] This hexagonal symmetry is further confirmed by the presence of a weak (210) peak previously reported at higher resolution at room

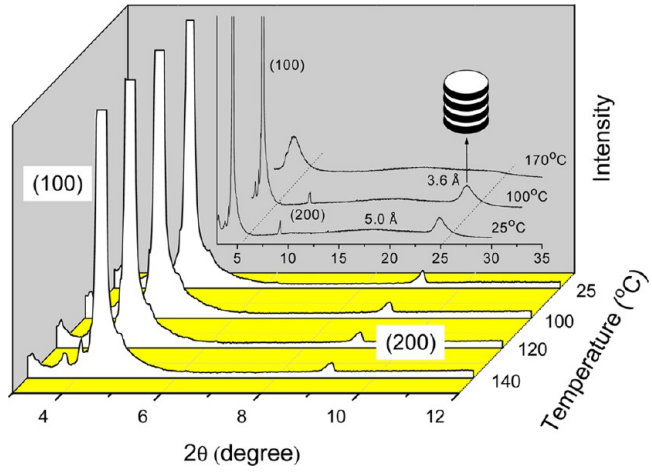

Figure 3. Temperature dependence of the first and second order columnar lattice peaks in the X-ray spectra. Inset: full XRD patterns in the isotropic phase at 170 °C, in the Col_h mesophase at 100 °C and at room temperature (25 °C).

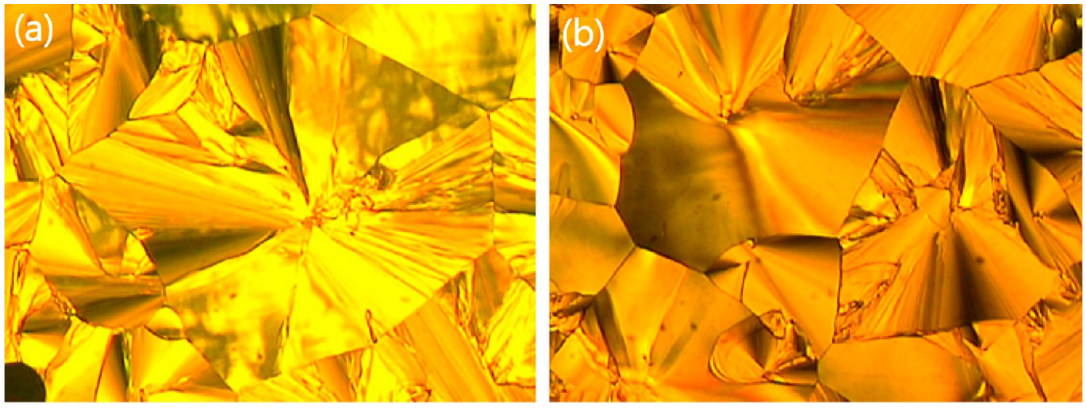

Figure 2. Optical microscopic images of focal conic texture. (a) at 120 °C and (b) at room temperature (25 °C). The textures were taken of the sample confined between two glass slides at a magnification of 100× (under crossed polarizers) with a CCD camera.

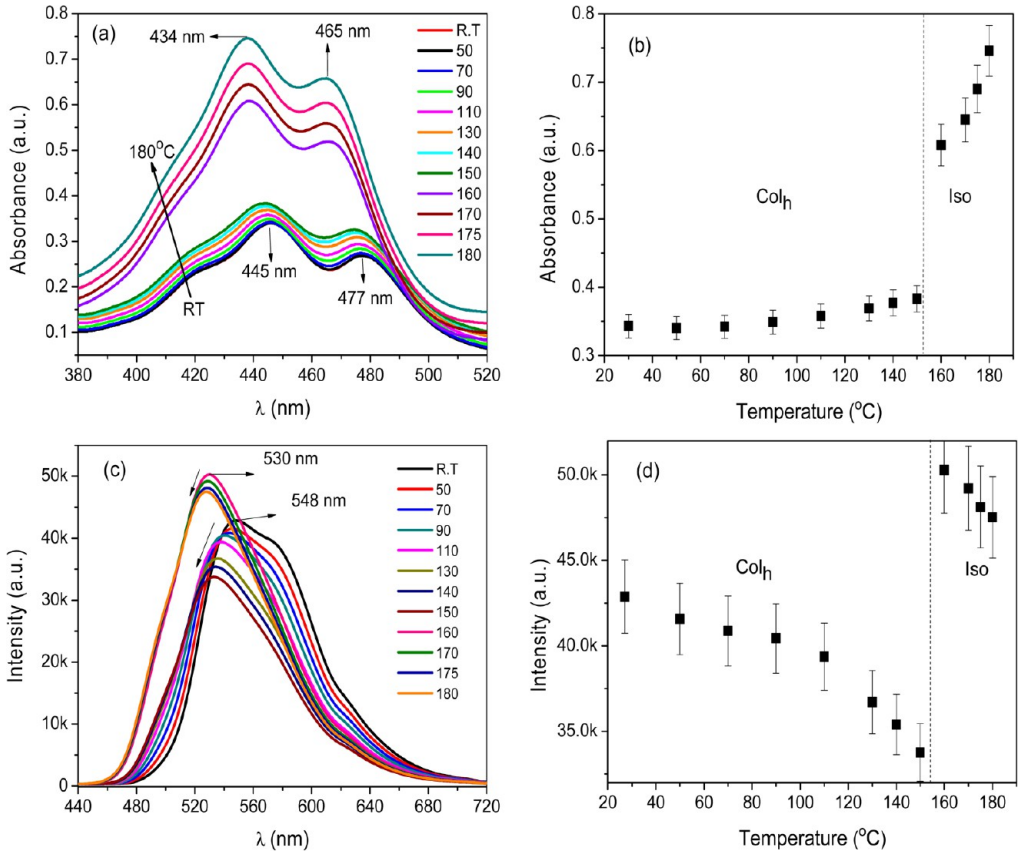

Figure 4. Absorbance (a) and photoluminescence (c) spectra recorded during heating from room temperature to the isotropic phase. Plot of the absorbance (b) and photoluminescence (d) at the wavelength of maximum intensity vs temperature.

temperature.[28] The 6-fold symmetry furthermore manifests itself directly in the domain shape at homeotropic growth, see Figure 5.

The Bragg-spacing values obtained from XRD data were d_{100} = 19.5 Å and d_{200} = 9.7 Å, respectively, where the lattice constant (a = 22.4 Å) was calculated from the position of the first maximum according to the equation $a = (2/3^{1/2})d_{100}$.[31]

In the wide angle region, the diffuse halo at 5.0 Å (2θ = 17.7°) indicates liquid-like ordered chains and the sharper peak at 2θ = 24.6° reveals an intracolumnar long-range order with a $\pi-\pi$ stacking distance of 3.6 Å, which suggests the presence of a short-range correlation within the columns, as illustrated in the inset of Figure 3. In addition, the appearance of this peak is especially important with respect to electronic conduction, since strong $\pi-\pi$ interactions are required for intermolecular order (overlap of orbitals), leading to an efficient charge carrier transport along the columns.[13]

The spectra presented in Figure 3 indicate that the intercolumnar spacings are not affected from 140 to 25 °C. The absence of new peaks in the wide angle region for 100 and 25 °C supports the lack of crystallization of the material at room temperature after cooling down from the isotropic phase (170 °C). The X-ray spectrum at 170 °C clearly shows that in the isotropic phase the hexagonal order is lost, due to the absence of the peaks at the low and wide angle regions, indicating a lack of translational and positional order of the molecules.

Photophysical Properties. The UV–vis absorption and photoluminescence spectra of ColLC films are presented in Figure 4. It is known from the literature that the molecules derived from perylenediimide present two well-defined bands of absorption in the visible region. These bands are attributed to the $n-\pi^*$ and $\pi-\pi^*$ transitions.[15,18,32]

At room temperature the compound showed strong absorption in the range of 380 to 500 nm with absorption peaks at 477 nm, 445 nm and a discrete shoulder at 422 nm, as shown in Figure 4a. The photoluminescence spectrum presents maximum emission intensity at 548 nm with a shoulder emission at 575 nm, see Figure 4c. Absorbance and photoluminescence were also measured as a function of temperature, with several spectra taken during heating cycles from room temperature to the isotropic phase as can be seen in Figures 4a and 4c.

The temperature-dependent absorbance spectra show a gradual increase of intensity with rising temperature across the Col$_h$ phase until 150 °C. At the Col$_h$-Iso transition, at approximately 155 °C, a discontinuity can be observed (see Figure 4a). As the temperature increases, the shoulder band at 422 nm becomes less prominent, nearly vanishing above the Col$_h$-Iso transition. A blue shift of the two main absorption peaks from 445 and 477 nm to 434 and 465 nm, respectively, is also observed in the analyzed range of temperatures. Those results are an evidence of the formation of aggregates due to strong intermolecular interactions in the mesophase.[33] It has been already mentioned by Schmidtke et al.[25] that perylenetetracarboxdiimide dyes present strong aggregation in the solid state, leading to modified absorption spectra dependent upon transverse and longitudinal offsets between molecules. A graph of the absorption at the wavelength of maximum intensity as a

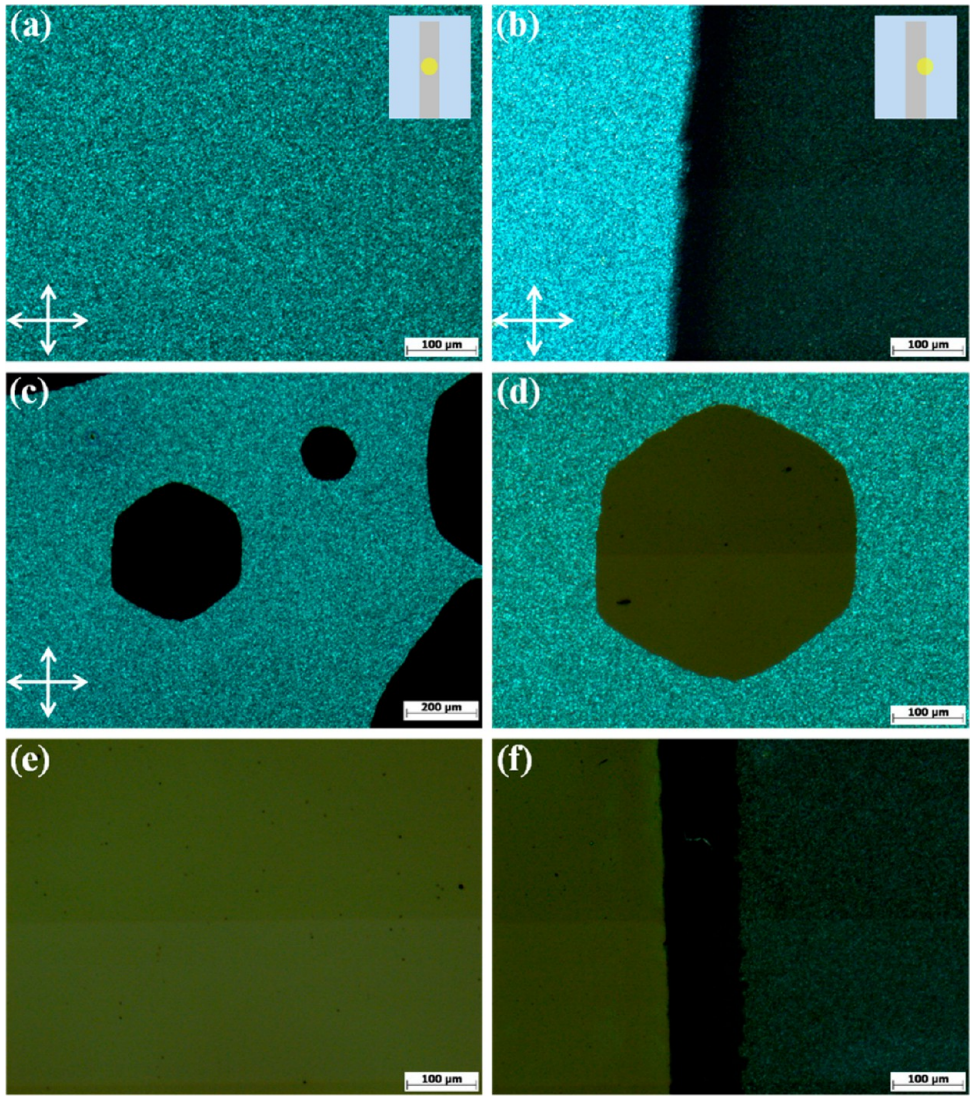

Figure 5. Optical images (100× magnification) obtained from POM showing the homeotropic alignment of the ColLC in the device structure: (a) under metal; (b) interface metal-free film; (c) after one hour at 120 °C under metal; (d) detail of the hexagonal germ; (e) after three hours at 120 °C under metal; and (f) interface metal-free film after cooling down to room temperature (25 °C). In the insets of parts a and b, the circle indicates the position under observation with respect to the metallic stripe.

function of the temperature is shown in Figure 4b, evidencing the strong increase of the absorbance at the Col_h-Iso transition.

Figure 4c shows the photoluminescence spectra at different temperatures. In the Col_h mesophase range it is possible to observe a reduction of the emission intensity with increasing temperature. The same behavior was found in the study of the temperature-dependent emission spectra of columnar triphenyltriazine derivatives published elsewhere.[34] This is expected for organic semiconductors due to a larger quantity of self-quenching aggregates and also due to nonradiative decay processes that are facilitated with increasing temperature.[34−39] At the Col_h-Iso transition a huge increase in emission intensity can be observed (Figure 4d). The lower emission in the Col_h phase is interpreted as due to the suppression of π-stacking aggregates, which are not present in the isotropic phase characterized by molecular disorder. The enhanced emission and the observed blue shift in the isotropic phase arise from the excited isolated molecules, where the exciton decays radiatively without exciton diffusion. Moreover, when the molecule is more isolated, its π-orbital is localized, giving rise to light emission with higher energy. To our knowledge, this is the first time that the effect of photoluminescence suppression in an ordered columnar phase was so clearly observed. Similar to the absorption spectra for increasing temperature the maximum emission peak presents a blue shift from 548 to 530 nm and the long wavelength shoulder at 575 nm is less evident, nearly vanishing above the Col_h-Iso transition. The same photophysical behavior was observed during the cooling from the isotropic phase to room temperature, confirming the reversibility of molecular aggregation interactions with temperature (see the Supporting Information).

Homeotropic Alignment. The homeotropic alignment (face-on orientation) of discotic molecules occurs usually during slow cooling from the isotropic melt at the transition to the liquid crystalline phase. Here, however, the homeotropic alignment was induced following an alternative procedure previously published, where samples are maintained at a temperature just below the isotropic transition for a few hours.[40] In contrast to previous work, where annealing was performed in an electrically inert glass/ColLC/Ag structure, in

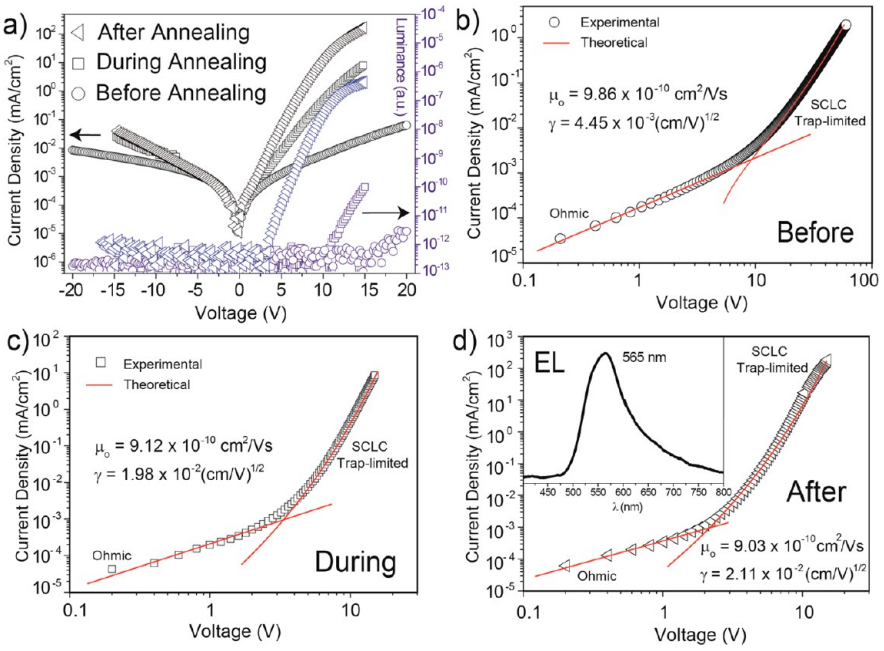

Figure 6. Electrical characterization of a spin-coated film in a diode structure. (a) Current density (left) and luminance (right) versus voltage. (b), (c), and (d) log–log plots of the *J-V* curves for the device before, during (120 °C for one hour), and after (120 °C for three hours) annealing, respectively. The solid lines indicate the fitting at the ohmic and at the trap-limited SCLC regimes. Inset of (d) shows the electroluminescence spectrum after annealing at a voltage of +15 V. Circles, squares, and triangles represent the device before, during, and after annealing, respectively.

the present work the face-on orientation was obtained via thermal annealing at 120 °C for three hours under a controlled N_2 atmosphere of a spin-coated thin film between typical device electrodes in an ITO/PEDOT:PSS/ColLC/Ca/Al structure. This allowed us to perform the electrical characterization on the same device, during and after annealing in order to correlate changes of electrical properties with molecule reorientation.

Figure 5 shows the sequence of the optical images captured via POM in reflection mode from the ITO side, where the schematic representation illustrates the metallic stripe evaporated on the film and the circle indicates the region under observation (inset of Figures 5a and 5b). Figures 5a, 5b, and 5c were taken under crossed polarizers, while in Figures 5d, 5e, and 5f the polarizers were slightly uncrossed for better viewing. Figure 5a shows the birefringent domains of the thin ColLC film under the metal layer, and Figure 5b shows the interface metal-free film, both taken before annealing at room temperature (25 °C). Figure 5c shows that, after one hour at 120 °C, the growth of nonbirefringent hexagonal domains has occurred under the metal layer, indicating the formation of the homeotropic alignment. Figure 5d shows in detail the hexagonal form of the domain. Homeotropically aligned samples typically do not show birefringence in POM between cross-polarizers, since the optical axis, in this case, coincidences with the columnar axis.[10] The hexagonal form asserts that the orientational transition is occurring within the hexagonal phase, and not at a phase transition to the isotropic state due to the confinement, where circular domains would be expected. Figure 5e shows that after three hours at 120 °C the whole film became homeotropically aligned under the metallic layer. The alignment remains even after cooling down to room temperature, as proven by Figure 5f, where the free film outside the metallic layer is still birefringent. Interestingly, the film was homeotropically oriented only under the metallic layer, indicating that the orientational transition requires strong confinement of the ColLC material between two solid interfaces.

Electrical Characterization. The device structure used for electrical characterization was ITO/PEDOT:PSS (45 nm)/ColLC (300 nm)/Ca (50 nm)/Al (100 nm). The thickness of the PEDOT:PSS (45 nm) and ColLC (300 nm) films were determined by a Dektak profilometer.

AFM measurements were performed to investigate the morphological aspects of the spin-coated films. From the measurements, the mean-surface-roughness (RMS) of the film was 2.5 nm for an image of 10 μm × 10 μm (see the Supporting Information for details). Electronic applications require homogeneous films with low surface roughness, so it is worth mentioning that such surface is considered smooth for technological applications.[13,34]

The electrochemical properties of the ColLC were investigated by cyclic voltammetry of a thin film coated on a Pt electrode (the cyclic voltammogram and details are presented in the Supporting Information). The LUMO has been determined to be at an energy level of −3.65 eV. The optical band gap (2.46 eV) was determined from the absorption spectrum,[41] and the HOMO level (−6.11 eV) estimated from the optical band gap and from the LUMO level. These values are comparable to those already published for perylene derivatives[8,15,18,20,42] and are in good agreement with results obtained by CV measurements in solution.[28]

The electrical measurements were performed at room temperature in a controlled N_2 atmosphere before, during (120 °C for one hour) and after (120 °C for three hours) the annealing process. Figure 6a shows the current-density/voltage (*J-V*) and luminance–voltage characteristics before (circles), during (squares) and after (triangles) annealing. Only a low degree of rectification in the *J-V* curve and a very low electroluminescence were observed for the nonannealed sample. Taking into account the energy diagram of our sample,

Table 1. Fitting Values Obtained for μ_0 and γ[a]

parameter/treatment	before annealing	during annealing	after annealing
μ_0 (10^{-10} cm^2/(V s))	(9.86 ± 0.03)	(9.12 ± 0.03)	(9.03 ± 0.03)
γ (10^{-2} cm$^{1/2}$/V$^{1/2}$)	(0.44 ± 0.02)	(1.98 ± 0.02)	(2.11 ± 0.02)
μ at V_Ω (cm^2/(V s))	(5.2 ± 0.2) × 10^{-8}	(2.5 ± 0.2) × 10^{-7}	(5.5 ± 0.1) × 10^{-7}
μ at applied +15 V (cm^2/(V s))	(8.8 ± 0.1) × 10^{-8}	(4.5 ± 0.1) × 10^{-4}	(8.5 ± 0.1) × 10^{-3}

[a]Using these fitting parameters the calculated mobilities for the corrected electric field at $V = V_\Omega$ and V = +15 V are presented.

one would expect a higher degree of rectification than that observed experimentally. The Ohmic characteristics (slope equal one in the log–log plot) observed for small voltages requires generally a net charge density of zero in the bulk of the sample. This can be achieved either by thermal excitation of electrons from the HOMO into the LUMO or by charge transfer doping. An estimation of the thermal excitation over the bandgap does, however, not generate enough free charge carriers. Such a generation could support a current density of about 5 × 10^{-19} mA/cm^2. In order to derive this value the Fermi-level of the material was assumed to be positioned at the center of the bandgap for a bandgap of E_g = 2.5 eV. In addition, a total density of states of 10^{21} cm^{-3}, a mobility of 10^{-7} cm^2 V^{-1} s^{-1} (as determined below), and an electric field strength of 5 V/300 nm were used. Since such an Ohmic current is much smaller than the measured one, it is possible to conclude that the organic semiconductor contains extrinsic charges most probably due to chemical doping by halogen ions or metal residues from synthesis.[13]

As can be seen from Figure 6a annealing introduces a higher degree of rectification compared to the nonannealed sample, approaching the shape of a typical diode. The current densities practically do not change in the Ohmic regime but increase by approximately 4 orders of magnitude at +15 V for the annealed device. This strong increase in rectification is almost certainly related to the homeotropic alignment of the columns, which provides a better π-orbital overlap and therewith a superior transport. To the authors' knowledge, such a degree of rectification and improvement of the *J-V* curves are unprecedented among perylenediimide derivatives, illustrating the benefits of columnar mesogenic ordering and macroscopically anisotropic mesophase alignment for the electronic performance.

The log–log plots of the current densities of the differently annealed samples are displayed in Figures 6b, 6c, and 6d. At low voltages all three curves follow an Ohmic behavior, obeying a power law of $J \propto V^n$ with $n \approx 1$, whereas at higher voltages, the injection of charge carriers from the electrodes becomes dominant and typical space charge effects are observed. The measured slopes of n = 2.9 up to 7.9 for the differently annealed samples indicate the existence of a density of states (DOS) which is altered by annealing. In the trap-free case one would expect a slope of n = 2 known as space-charge limited current (SCLC) obeying the well-known Mott-Gurney law[43−45]

$$J = \frac{9}{8}\varepsilon\varepsilon_0\mu\frac{V^2}{L^3} \tag{1}$$

with $\varepsilon\varepsilon_0$ the permittivity of the organic film, μ the charge carrier mobility, and L the film thickness. In order to model the experimentally observed SCLC the charge transport will be described by a hopping conduction through this DOS originally described by Bassler et al.[46] He assumes that the complicated motion of the charge carrier in a disordered solid can be described solely by a field dependence of the mobility within a Gaussian DOS according to the following relation also used by others[47−51]

$$\mu = \mu_0^* e^{-\left(\frac{2\sigma}{3kT^2}\right)} e^{\gamma\sqrt{E}} = \mu_0(T) e^{\gamma\sqrt{E}} \tag{2}$$

where μ_0^* is a constant, σ is the width of the DOS, k is the Boltzmann constant, T is the temperature, and E is the electric field. γ resembles a Poole-Frenkel coefficient which accounts for the asymmetry of the potential wells generated by electric field E. The steady-state trap-limited SCLC can now be derived by substituting the field dependent mobility of eq 2 into the current equation

$$J = n(x, T)e\mu(E, T)E(x) \tag{3}$$

which can be solved by utilizing Poisson's equations

$$\frac{\epsilon}{e}\frac{dE(x)}{dx} = n(x, T) \tag{4}$$

together with the boundary condition $E(0) = 0$. Combining eqs 2, 3, and 4 the resulting differential equation can be analytically integrated, giving rise to the following relation between the location x and the electric field strength E:

$$x = 2\frac{\varepsilon\varepsilon_0}{J}\mu_0\frac{1}{\gamma^4}(6 + e^{\gamma\sqrt{E}}\gamma^3E^{3/2} - 3\gamma^2Ee^{\gamma\sqrt{E}} + 6\gamma\sqrt{E}\,e^{\gamma\sqrt{E}} - 6e^{\gamma\sqrt{E}}) \tag{5}$$

The final J/V relation is then obtained by integrating the electric field E with respect to x, which can be solved by integration by parts

$$V = \int_0^L E(x)dx = Ex|_0^L - \int_0^{E_L} x(E)dE \tag{6}$$

where E_L is the electric field at the counter electrode, which can be calculated by determining the roots of eq 5 for $x = L$.

Such integration was performed for ε = 3.0 (obtained by capacitance measurements, see the Supporting Information), and the thickness of the organic layer L = 300 nm. Thereby values for μ_0 and γ were extracted from fitting the theoretical *J-V* curves to the experimental ones. It should be noted that the SCLC currents are only fitted to the difference of the measured current and the linearly extrapolated Ohmic currents. For the above-discussed calculation of the charge carrier density in the Ohmic regime, μ of the SCLC at the crossing point V_Ω was utilized since it should not change just because of the change in the transport mechanism. The average value of this mobility amounts to 1.10^{-7} cm^2 V^{-1} s^{-1} with a spread of 1 order of magnitude possibly due to differences in the annealing process, see Table 1. Fits are shown for each annealing stage (before, during, and after annealing) in Figures 6b, 6c, and 6d, respectively. The respective fitting interval in voltage was taken from the experiment reaching from right above the kink in the log–log current/voltage characteristic (transition from Ohmic to SCLC region) up to the highest voltage applied in

order not to violate the validity region of eq 2. From the kinks in the plots one can determine the onset voltages (V_Ω) between the Ohmic and trap-limited SCLC regimes, being approximately at +9.8 V, +3.2 V, and +2.0 V for the nonannealed, partially annealed, and annealed case, respectively. The fitting of the SCL current densities displayed in Figures 6b, 6c, and 6d show a very good agreement with experimental data with fitting parameters listed in Table 1.

By adding the Ohmic region it is possible to fit the whole experimental curves. The Poole-Frenkel coefficients γ increase with annealing, revealing that the hopping transport is made easier in the annealed sample than in the partially annealed and the nonannealed ones.

From eq 2 it is obvious that due to the annealing a large increase in charge carrier mobility is achieved in the SCLC region which reaches about 5 orders of magnitude. In Table 1 are presented the values calculated for each annealing step for the corrected electric field related to the applied voltage of +15 V, see also the graphs of $\mu(V)$ in the Supporting Information. It should also be mentioned that this increase in mobility is responsible for the related increase in SCLC current density which explains the shift in the turn-on voltage V_Ω to smaller values due to the experimental fact that the Ohmic currents are almost unchanged after the different annealing steps. V_Ω for the differently annealed devices shifts from +15 V before annealing, to +10 V for partial annealing, to +3.5 V for a complete annealing.

It is also interesting to investigate the onset of the electroluminescence. As can be seen from Figure 6 this onset happens at slightly higher applied voltages than the respective V_Ω. The reason therefore most likely can be seen in an increased electric field at the counter electrode which is a consequence of the SCLC transport. Such an enhanced electric field gives rise to a thinner injection barrier for holes which then can be crossed by quantum-mechanical tunneling. The subsequent recombination of electrons and holes results in light emission. The respective field strengths at the hole injecting electrode for all differently annealed samples are approximately at 7×10^7 V/m (at 15 V).

4. CONCLUSION

The characterization of a perylenediimide derivative is presented in view of its application as active organic layer in diode structures. The strength of the investigated material is the existence of a columnar hexagonal liquid crystalline phase at room temperature together with a convenient transition temperature to the isotropic liquid state that allows annealing close to the phase transition temperature. The thermal stability of the hexagonal columnar liquid crystalline phase and of the molecular structure was established by thermal DSC and TGA analysis, polarizing optical microscopy, and X-ray diffraction. Temperature dependent absorption and fluorescence measurements taken in the isotropic liquid state and in the mesophase down to room temperature clearly corroborate a pronounced quenching of fluorescence by π-stacking in the organized columnar structure. The face-on organization was successfully induced within metallic contacts by annealing the device for three hours at a temperature of 120 °C, below that of the isotropic transition, in a diode configuration.

The annealing process resulted in pronounced improvement of the electrical properties. The *J-V* characteristics revealed an initial Ohmic behavior at low voltages that above V_Ω evolves into a SCLC regime. The SCLC transport was modeled assuming a Poole-Frenkel like field dependence of the charge carrier mobility. The modeled results could be interpreted by associating the annealing processes to the disorder parameter extracted from the mobility at zero fields. It was found that annealing narrows the width of the Gaussian distribution, thereby improving charge carrier transport by 4 orders of magnitude in current and 5 orders of magnitude in charge carrier mobility. It is inferred that the SCLC character of the transport of the columnar structure allows for an improved charge injection of the holes at the counter electrode and therewith allowing for light emission. Macroscopically uniform homeotropic alignment by postfabrication annealing of diode structures with a columnar mesogenic emitter material is thus shown to improve current rectification, charge mobility, and electroluminescence dramatically.

■ ASSOCIATED CONTENT

Ⓢ Supporting Information

Thermal stability measurement (TGA), the absorption and emission spectra of thin films as a function of the temperature during the cooling cycle, AFM analysis of the spin-coated film, cyclic voltammetry for the HOMO/LUMO determination, AC impedance measurements, and the charge mobilities at the SCLC regime as a function of the voltage for the device before, during, and after annealing. This material is available free of charge via the Internet at http://pubs.acs.org.

■ AUTHOR INFORMATION

Corresponding Author

*Phone: +55 48 37219761. Fax: +55 48 37219946. E-mail: ivan.bechtold@ufsc.br.

Notes

The authors declare no competing financial interest.

■ ACKNOWLEDGMENTS

The authors thank the following institutions for financial support: CAPES, CNPq, and INCT/INEO. The XRD experiments were carried out in the Laboratório de Difração de Raios-X (LDRX-CFM/UFSC). The authors are grateful to Dr. Paula C. Rodrigues for the cyclic voltammetry analysis. G.C.F. acknowledges the fellowship by the "Fundação de Amparo à Pesquisa do Estado de São Paulo" (FAPESP) (Proc-number 2008/01935-5 and 2012/01303-4) and by the "Deutscher Akademischer Austauschdienst" (DAAD) (A/09/72945; ref 415). H.v.S. acknowledges the scholarship "Special Visiting Researcher" by the Brazilian Science without Borders Program (CNPq and Capes − Proc-number 400133/2012-1).

■ REFERENCES

(1) Leng, S.; Chan, L. H.; Jing, J.; Hu, J.; Moustafa, R. M.; Horn, R. M.; Graham, M. J.; Sun, B.; Jeong, K.-U.; Kaafarani, B. R.; Zhang, W.; Harris, F. W.; Cheng, S. Z. D. *Soft Matter* **2010**, *6*, 100−112.

(2) Iino, H.; Hanna, J. *Opto-Electron. Rev.* **2005**, *13*, 295−302.

(3) Kaafarani, B. R. *Chem. Mater.* **2011**, *23*, 378−396.

(4) Bushby, R. J.; Kawata, K. *Liq. Cryst.* **2011**, *38*, 1415−1426.

(5) Pisula, W.; Zorn, M.; Chang, J. Y.; Müllen, K.; Zentel, R. *Macromol. Rapid Commun.* **2009**, *30*, 1179−1202.

(6) Hayashi, H.; Nihashi, W.; Umeyama, T.; Matano, Y.; Seki, S.; Shimizu, Y.; Imahori, H. *J. Am. Chem. Soc.* **2011**, *133*, 10736−10739.

(7) Haverkate, L. A.; Zbiri, M.; Johnson, M. R.; Deme, B.; Groot, H. J. M.; Lefeber, F.; Kotlewski, A.; Picken, S. J.; Mulder, F. M.; Kearleys, G. J. *J. Phys. Chem. B* **2012**, *116*, 13098−13105.

(8) Wicklein, A.; Muth, M.-A.; Thelakkat, M. *J. Mater. Chem.* **2010**, *20*, 8646−8652.

(9) O'Neill, M.; Kelly, S. M. *Adv. Mater.* **2011**, *23*, 566−584.
(10) Segeyev, S.; Pisula, W.; Geerts, Y. H. *Chem. Soc. Rev.* **2007**, *36*, 1902−1929.
(11) Funahashi, M.; Hanna, J.-I. *Chem. Phys. Lett.* **2004**, *397*, 319−323.
(12) O'Neill, M.; Kelly, S. M. *Adv. Mater.* **2003**, *15*, 1135−1146.
(13) Bechtold, I. H.; Eccher, J.; Faria, G. C.; Gallardo, H.; Molin, F.; Gobo, N. R. S.; Oliveira, K. T.; Seggern, H. *J. Phys. Chem. B* **2012**, *116*, 13554−13560.
(14) Liu, S.-G.; Sui, G.; Cormier, R. A.; Leblanc, R. M.; Gregg, B. A. *J. Phys. Chem. B* **2002**, *106*, 1307−1315.
(15) Yang, L.; Shi, M.; Wang, M.; Chen, H. *Tetrahedron* **2008**, *64*, 5404−5409.
(16) Newman, C. R.; Frisbie, C. D.; da Silva Filho, D. A.; Brédas, J.-L.; Ewbank, P. C.; Mann, K. R. *Chem. Mater.* **2004**, *16*, 4436−4451.
(17) Strijk, C. W.; Sieval, A. B.; Dakhorst, J. E. J.; Dijk, M.; Kimkes, P.; Koehorst, R. B. M.; Donker, H.; Schaafsma, T. J.; Picken, S. J.; van de Craats, A. M.; Warman, J. M.; Zuilhof, H.; Sudholter, E. J. R. *J. Am. Chem. Soc.* **2000**, *122*, 11057−11066.
(18) Erten, S.; Meghdadi, F.; Gunes, S.; Koeppe, R.; Sariciftci, N. S.; Icli, S. *Eur. Phys. J. Appl. Phys.* **2007**, *36*, 225−229.
(19) Seguy, I.; Destruel, P.; Bock, H. *Synth. Met.* **2000**, *111−112*, 15−18.
(20) Seguy, I.; Jolinat, P.; Destruel, P.; Farenc, J.; Mamy, R.; Bock, H.; Ip, J.; Nguyen, T. P. *J. Appl. Phys.* **2001**, *89*, 5442−5448.
(21) Chesterfield, R. J.; McKeen, J. C.; Newman, C. R.; Ewbank, P. C.; da Silva Filho, D. A.; Brédas, J.-L.; Miller, L. L.; Mann, K. R.; Frisbie, C. D. *J. Phys. Chem. B* **2004**, *108*, 19281−19292.
(22) Schon, J. H.; Kloc, C.; Batlogg, B. *Appl. Phys. Lett.* **2000**, *77*, 23.
(23) Dimitrakopoulos, C. D.; Malenfant, P. R. L. *Adv. Mater.* **2002**, *14*, 99−117.
(24) Schmidt-Mende, L.; Fechtenkotter, A.; Mullen, K.; Moons, E.; Friend, R. H.; Mackenzie, J. D. *Science* **2001**, *293*, 1119−1122.
(25) Schmidtke, J. P.; Friend, R. H.; Kastler, M.; Mullen, K. *J. Chem. Phys.* **2006**, *124*, 174704.
(26) Oukachmih, M.; Destruel, P.; Seguy, I.; Ablart, G.; Jolinat, P.; Archambeau, S.; Mabiala, M.; Fouet, S.; Bock, H. *Sol. Energy Mater. Sol. Cells* **2005**, *85*, 535−543.
(27) Marcon, V.; Breiby, D. W.; Pisula, W.; Dahl, J.; Kirpatrick, J.; Patwardhan, S.; Grozema, F.; Andrienko, D. *J. Am. Chem. Soc.* **2009**, *131*, 11426−11432.
(28) Kelber, J.; Achard, M.-F.; Garreau-de Bonneval, B.; Bock, H. *Chem. Eur. J.* **2011**, *17*, 8145−8155.
(29) Omenat, A.; Barbera, J.; Serrano, J. L.; Houbrechts, S.; Persoons, A. *Adv. Mater.* **1999**, *11*, 1292−1295.
(30) Wen, C.-R.; Wang, Y.-J.; Wang, H.-C.; Sheu, H.-S.; Lee, G.-H.; Lai, C. K. *Chem. Mater.* **2005**, *17*, 1646−1654.
(31) Gallardo, H.; Ferreira, M.; Vieira, A. A.; Westphal, E.; Molin, F.; Eccher, J.; Bechtold, I. H. *Tetrahedron* **2011**, *67*, 9491−9499.
(32) Wang, N.; Li, Y.; He, X.; Gan, H.; Li, Y.; Huang, C.; Xu, X.; Xiao, J.; Wang, S.; Liu, H.; Zhu, D. *Tetrahedron* **2006**, *62*, 1216−1222.
(33) Egbe, D. A. M.; Turk, S.; Rathgeber, S.; Kuhnlenz, F.; Jadhav, R.; Wild, A.; Birckner, E.; Adam, G.; Privrikas, A.; Cimrova, V.; Knor, G.; Sariciftci, N. S.; Hoppe, H. *Macromolecules* **2010**, *43*, 1261−1269.
(34) Cristiano, R.; Eccher, J.; Bechtold, I. H.; Tironi, C. N.; Vieira, A. A.; Molin, F.; Gallardo, H. *Langmuir* **2012**, *28*, 11590−11598.
(35) Giménez, R.; Piñol, M.; Serrano, J. L. *Chem. Mater.* **2004**, *16*, 1377−1383.
(36) Yelamaggad, C. V.; Achalkumar, A. S.; Rao, D. S. S.; Prasad, S. K. *J. Org. Chem.* **2009**, *74*, 3168−3171.
(37) Liao, C. T.; Chan, H. H.; Hsu, F.; Poloek, A.; Yeh, H. H.; Chi, Y.; Wang, K. W.; Lai, C. H.; Lee, G. H.; Shih, C. W.; Chou, P. T. *Chem. Eur. J.* **2011**, *17*, 546−556.
(38) Venuti, E.; Valle, R. G. D.; Bilotti, I.; Brillante, A.; Cavallini, M.; Calo, A.; Geerts, Y. H. *J. Phys. Chem. C* **2011**, *115*, 12150−12157.
(39) Sasson, R.; Draitbart, O.; Weinreb, A. *J. Lumin.* **1988**, *40−41*, 207−208.
(40) Brunet, T.; Thiebaut, O.; Charlet, E.; Bock, H.; Kelber, J.; Grelet, E. *Europhys. Lett.* **2011**, *93*, 16004.
(41) Hellstrom, S.; Zhang, F.; Inganas, O.; Andersson, M. R. *Dalton Trans.* **2009**, 10032−10039.
(42) An, Z.; Yu, J.; Jones, S. C.; Barlow, S.; Yoo, S.; Domercq, B.; Prins, P.; Siebbeles, L. D. A.; Kippelen, B.; Marder, S. *Adv. Mater.* **2005**, *17*, 2580−2583.
(43) Mott, N. F.; Gurney, D. *Electronic Processes in Ionic Crystals*; Academic Press: New York, 1970; p 45.
(44) Murgatroyd, P. N. *J. Phys. D: Appl. Phys.* **1970**, *3*, 151.
(45) Campbell, A. J.; Bradley, D. D. C.; Lidzey, D. G. *J. Appl. Phys.* **1997**, *82*, 6326.
(46) Bassler, H. *Phys. Status Solidi B* **1993**, *175*, 15−56.
(47) Lupton, J. M.; Samuel, I. D. W. *J. Phys. D: Appl. Phys.* **1999**, *32*, 2973−2984.
(48) Lupton, J. M.; Samuel, I. D. W. *Synth. Met.* **2000**, *111−112*, 381−384.
(49) Blom, P. W. M.; de Jong, M. J. M.; van Munster, M. G. *Phys. Rev. B* **1997**, *55*, R656−R659.
(50) Bozano, L.; Carter, S. A.; Scott, J. C.; Malliaras, G. G.; Brock, P. J. *Appl. Phys. Lett.* **1999**, *74*, 1132−1134.
(51) Fleissner, A.; Schmid, H.; Melzer, C.; von Seggern, H. *Appl. Phys. Lett.* **2007**, *91*, 242103.